X-ray−Neutron Study of the Electron Density in Diammonium Hexaaquairon(II) Disulfate-d_{20} at 10.5 K and the Success of Ligand Field Modeling

B. N. Figgis,[†] A. N. Sobolev,[†] D. M. Young,[§] A. J. Schultz,[§] and P. A. Reynolds*[,‡]

Contribution from the Department of Chemistry, University of Western Australia, Nedlands, W.A. 6009, Australia, Research School of Chemistry, Australian National University, Canberra, ACT 0200, Australia, and Intense Pulsed Neutron Source, Argonne National Laboratory, Argonne, Illinois 60439-4814

Received November 20, 1997

Abstract: We have obtained an X-ray diffraction data set at 10.5(5) K and a neutron diffraction data set at 12(2) K for the title compound. The atomic positional and displacement parameters derived from the two data sets agree satisfactorily, as the very low temperatures markedly reduce systematic errors. In the partial X-ray−neutron analysis of the X-ray data it was necessary to use a multipole model that introduces additional flexibility in the radial functions for valence orbitals of atoms. The electron density around the iron site is compared with that produced by a ligand-field model which has been used to interpret and collate a number of measurements of physical properties of the compound. Good agreement is obtained for the shape and orientation of the 3d density, but there are some quantitative differences. There are large 4p densities, due to covalent transfer from the ligating water molecules. We confirm on the one hand the ability of the X-ray experiment to give detailed chemically relevant information and on the other hand that, with care, ligand-field theory may be used in the quantitative prediction of transition metal ion physical properties.

Introduction

The study of the electron density in crystals containing molecules of transition metal complexes is an independent method for their examination in real space and complements spectroscopic results and *ab initio* theories. In some cases the X-ray diffraction experiments give electron densities which coincide well with theoretical calculations performed on the relevant molecules and provide chemically useful information; see for example refs 1−4. These are cases in which the ground state is not in doubt due to the combination of metal oxidation state and ligand field size and symmetry.

However, there are often cases where the molecular ground state is not obvious. This may arise because the major components of the ligand field do not lift the metal ion orbital degeneracy sufficiently that we can neglect spin−orbit coupling of the lowest lying states. This is clearly a more serious problem with the heavier transition metals, but also often occurs in the first transition series when the true metal ion site symmetry is low but approximates to a higher symmetry. *Ab initio* theories still cannot routinely deal with spin−orbit coupling. As a result, even now, recourse must be made to ligand-field theory or the related (but theoretically more respectable) angular overlap models.[5]

We may ask an old, but still relevant, question of ligand-field theory: does it have predictive power, or is it merely a convenient method of parametrizing a restricted set of results? If it can, in fact, be used to provide insights into the electronic structure of the metal complex then it is more truly useful. A simple property that ligand-field theory predicts is the ground-state 3d electron density. An X-ray diffraction experiment can measure this, and it provides a test well outside the normal range of spectroscopic experiments. This paper attempts such a test.

The choice of a system for study is relatively straightforward. We must select a compound where the ligand-field model is complete and general—which often is not the case. In addition, the diffraction experiment, to be convincing, needs to be of the best possible quality on a relatively simple and well-studied system with no underlying difficulties such as phase transitions or other anomalous crystallographic behaviors. Tutton salts, the hydrated double sulfates of a mono- and a divalent cation, are obvious candidates.

An example of a Tutton salt is diammonium hexaaquacopper-(II) disulfate (ammonium copper Tutton salt (CuTS)), which contains hexaaquacopper(II) and ammonium and sulfate fragments hydrogen bonded into a lattice framework. For it there is good-quality experimental electron density information obtained by combination of X-ray and neutron diffraction. The measurements were at ca. 10 and 15 K, to minimize systematic defects in such determinations, specifically high thermal motion, anharmonicity, and thermal diffuse scattering, which are present at higher temperatures.[4] The large Jahn−Teller distortion in this salt ensures a simple predictable ground state. A good-

[†] University of Western Australia.
[‡] Australian National University.
[§] Argonne National Laboratory.
* Author to whom correspondence should be addressed.

(1) Presprich, M. R.; White, M. A.; Vekhter, Y.; Coppens, P. *J. Am. Chem. Soc.* **1994**, *116*, 5233−5238.
(2) Antipin, M. Yu.; Tsirel'son, V. G.; Flyugge, M. P.; Stuchkov, Yu. T.; Ozerov, R. P. *Sov. J. Coord. Chem.* **1987**, *13*, 67−75.
(3) Smith, G. T.; Mallinson, P. R.; Frampton, C. S.; Farrugia, L. J.; Peacock, R. D.; Howard, J. A. K. *J. Am. Chem. Soc.* **1997**, *119*, 5028−5034.
(4) Figgis, B. N.; Iversen, B. B.; Larsen, F. K.; Reynolds, P. A. *Acta Crystallogr., Sect. B* **1993**, *49*, 794−806.
(5) Gerloch, M. *Magnetism and Ligand Field Analysis*; Cambridge University Press: Cambridge, U.K., 1983.

S0002-7863(97)03980-2 CCC: $15.00
Published on Web 08/18/1998

quality *ab initio* calculation of the X-ray structure factors as a sum of free ND_4^+, SO_4^{2-}, and $Cu(OD_2)_6^{2+}$ contributions has been performed. It agrees well, although not quite perfectly, with the experimental data, not only in gross 3d orbital populations, but also in more subtle details of radial distributions, overlap densities, and covalence.[6]

CuTS has a large Jahn−Teller distortion of the hexaaquacopper(II) fragment which ensures little doubt about a simple 3d configuration for the ground state. Such is not the case with the isomorphous ammonium ferrous Tutton salt (FeTS), which contains the $Fe(OH_2)_6^{2+}$ ion. This ion is Jahn−Teller susceptible, but there is only small structural distortion even at 4.3 K.[7] The $t_{2g}^4e_g^2$ 3d electronic configuration of the free Fe(II) ion in octahedral symmetry, neglecting spin−orbit coupling, is a 15-fold degenerate $^5T_{2g}$ state. Theoretical *ab initio* calculations at the experimental FeTS geometry[8] but neglecting spin−orbit coupling show, as expected, three near-degenerate spin-quintet states split by the small geometrical distortion from octahedral. These three approximately place the fourth t_{2g} electron in each of the *xy*, *xz*, and *yz* 3d orbitals, with only small mixing of the other two t_{2g} functions. However, as these three sets of degenerate quintet states are calculated to lie within ca. 200 cm^{-1} of each other it is not permissible to neglect spin−orbit coupling, since the coupling constant, ζ, is ca. 400 cm^{-1}. As relativistic molecular calculations of such a system are not yet feasible, we must resort to empirical ligand-field models for a theoretical account of the ground-state 3d electron density distributions, in particular the mixing amonst the 3d t_{2g} orbitals induced by spin−orbit coupling. Such models introduce a treatment of covalence only in an *ad hoc* parametric fashion.

There exists already such a ligand-field model for FeTS[9] which reproduces many experimental results for the compound, often involving single crystal data. Included are specific heat, inelastic neutron scattering, far-IR magnetic resonance, magnetic susceptibilities, and Mossbauer spectra (see ref 9 and references therein). This model assumes ONLY the true crystallographic inversion symmetry of the iron site and makes NO assumptions about any of its possible parameters. It is thus as complete as such a model can be. The eight-parameter model predicts *inter alia* electron density in the ground state and magnetic properties observable by polarized neutron diffraction (PND). We note that five low-lying states at zero magnetic field are predicted with relative energies 0, 6.4, 29.0, 94.0, and 99.2 cm^{-1}. The next 10 states are at higher energies, spread between 292.1 and 719.8 cm^{-1}.

To support our program of X-ray and PND studies of Tutton salts (see ref 6 for references), we previously completed a neutron structure determination at 4.3 K,[7] PND at 4.3 K,[10] and an X-ray charge density study at 85 K[11] on FeTS. There has also been a further room-temperature structure determination for purposes of comparison across the first transition metal series[12] and theoretical studies of the electronic structure of the hexaaquairon(II) ion.[13−15] The PND results are complex, and we have not yet been able to fully reconcile the ligand-field model with them,[16] partly because of the difficulties introduced by the orbital angular momentum contribution to the magnetic scattering. The X-ray diffraction is in this case simpler to interpret. At 85 K the temperature is high enough that the ground state is estimated to contribute only ca. 33% of the observed density. In the present work we have proceeded to a clearer and more definitive test by obtaining X-ray diffraction data at very low temperatures. We have also repeated the determination of the structure by neutron diffraction with a more accurate and extensive data set, since it became apparent that the earlier result may contain some small systematic error that we do not want to cloud our present study.

For FeTS by X-ray diffraction at 10.5 K in this paper we directly examine the electron distribution dominated by the ground state, and this provides a powerful constraint on its nature. The previous ligand-field modeling prediction of 3d density is shown to be qualitatively correct but slightly quantitatively defective, and we can also add extra bonding features not due to 3d electrons. This ability to examine such a fundamental property as the crystal electron distribution of the ground state by X-ray diffraction is thus seen to be of considerable chemical relevance.

Experimental Section

Pale green deuterated crystals of diammonium hexaaquairon(II) disulfate-d_{20}, $[ND_4]_2[Fe(D_2O)_6](SO_4)_2$, were prepared by recrystallization of the hydrogenous salt from faintly acidic D_2O solution. They were of typical platy morphology ({110}, {001}) and were used in the X-ray and neutron diffraction experiments.

Neutron Diffraction Data Collection and Refinement. A data set was collected at 10.2−13.8 K using a single crystal mounted in an Air Products Displex refrigerator on the single crystal time of flight neutron diffractometer at the Intense Pulsed Neutron Source (IPNS) of the Argonne National Laboratory. Experimental details are collected in Table 1 and are described in more detail elsewhere.[17] The structure was refined using local IPNS software.[17] The derived positional and displacement parameters are given in Table 2. The degree of deuteration refined to 91.8(3)%.

The derived structure is an improvement on that of Figgis *et al.*[10] The standard uncertainties are decreased by a factor of 2−3, allowing more critical comparison with the X-ray results. More importantly, a low sulfur average displacement parameter and low U_{13} elements of the displacement tensor for all non-hydrogen atoms are no longer present. If we compare the present with the previous results, while the deuterium displacement parameters agree well, those for the other atoms show a rather uniform pattern of differences: U_{11}, U_{22}, U_{33}, and U_{13} are low and U_{12} is high. The shifts are in the range 0.001−0.002 $Å^2$, which while quite small are noticeable because of the high precision of our 10 K X-ray results. It appears that the previous neutron data contain some small systematic error. The high maximum $\sin\theta/\lambda$ of 1.15 $Å^{-1}$ of this time-of-flight spallation source data compared to the previous normal, reactor-based, neutron data also provides the important constraint that no anharmonic Gram−Charlier parameter c_{hjk} or c_{hjkl} can exceed 2×10^{-5}.

X-ray Diffraction Data and Refinement. A full sphere data set at 10.5 K was collected using a locally assembled X-ray diffractometer with a type 512 Huber goniometer equipped with a Displex DE-202

(6) Chandler, G. S.; Figgis, B. N.; Reynolds, P. A.; Wolff, S. K. *Chem. Phys. Lett.* **1994**, *225*, 421−426.
(7) Figgis, B. N.; Kucharski, E. S.; Reynolds, P. A.; Tasset, F. *Acta Crystallogr., Sect C* **1989**, *45*, 942−944.
(8) Chandler, G. S.; Christos, G. A.; Figgis, B. N.; Reynolds, P. A. *J. Chem. Soc., Faraday Trans. 2* **1992**, *88*, 1961−1969.
(9) Doerfler, R. *J. Phys. C* **1987**, *20*, 2533−2542.
(10) Figgis, B. N.; Forsyth, J. B.; Kucharski, E. S.; Reynolds, P. A.; Tasset, F. *Proc. R. Soc. London A* **1990**, *428*, 113−127.
(11) Figgis, B. N.; Kepert, C. J.; Kucharski, E. S.; Reynolds, P. A. *Acta Crystallogr., Sect B* **1992**, *48*, 753−761.
(12) Cotton, F. A.; Daniels, L. M.; Murillo, C. A.; Quesada, J. F. *Inorg. Chem.* **1993**, *32*, 4861−4867.
(13) Akesson, R.; Pettersson, L. G. M.; Sandstrom, M.; Siegbahn, P. E. M.; Wahlgren, U. *J. Phys. Chem.* **1992**, *96*, 10773−10779.
(14) Mandix, K.; Johansen, H. *J. Phys. Chem.* **1992**, *96*, 7261−7265.
(15) Akesson, R.; Pettersson, L. G. M.; Sandstrom, M.; Wahlgren, U. *J. Am. Chem. Soc.* **1994**, *116*, 8691−8704.
(16) Delfs, C. D. Ph.D. Thesis, University of Western Australia, 1991.
(17) Schultz, A. J.; Srinivasean, K.; Teller, R. G.; Williams, J. M.; Lukehart, C. M. *J. Am. Chem. Soc.* **1984**, *106*, 999−1003.

Table 1. Experimental Data for $(ND_4)_2Fe(SO_4)_2 \cdot 6D_2O$

	X-ray	neutron
radiation (λ)	Mo Kα (0.7107)	time-of-flight, 0.7−4.2
temp (K)	10.5(5)	12(2)
crystal size (mm)	0.67 × 0.61 × 0.33	5.0 × 5.0 × 2.0
empirical formula	$D_{20}O_{14}N_2S_2Fe$	$D_{20}O_{14}N_2S_2Fe$
formula weight	412.16	412.16
F(000) (e)	437.6	
crystal system	monoclinic	monoclinic
space group	$P2_1/a$	$P2_1/a$
Z	2	2
D_c (Mg m^{-3})	1.99	1.99
μ (mm^{-1})	1.47	$0.0546 + 0.0012\lambda$
a (Å)	9.161(1)	9.161[a]
b (Å)	12.409(1)	12.409[a]
c (Å)	6.305(1)	6.305[a]
β (deg)	106.69(1)	106.69[a]
volume (Å^3)	686.6(1)	686.6[a]
max sin θ/λ (Å^{-1})	1.08	1.15, all to 0.85
h range	−19 to 19	−19 to 7
k range	−26 to 26	−27 to 4
l range	−13 to 13	−9 to 14
no. of reflns colld	29764	6316
no. of ind reflns	7159	
R(int)	0.014	no averaging
transmission(max)	0.6057	0.8295
transmission(min)	0.4907	0.7519
no. of parameters	274	202
GOF (on F^2)	1.175	1.176
$R(F)$ ($I > 3\sigma(I)$)	0.0096	0.0442
$wR(F^2)$ (all data)	0.0212	0.0845
$R(F^2)$ (all data)	0.0166	0.04115
$\Delta\rho$(max) (e Å^{-3})	0.20	
$\Delta\rho$(min) (e Å^{-3})	−0.20	

[a] The X-ray-defined values were adopted, as they are more accurate than can be obtained from the neutron diffraction experiment.

cryorefrigerator, patterned after the machine of Henriksen *et al.*[18] It uses filtered Mo Kα X-ray radiation. The procedures used follow those detailed previously for CuTS,[4] and so here we give only a short description. Collection of three standard reflections from every 100 showed negligible crystal deterioration. Other experimental details are collected in Table 1. Locally written diffractometer software was used for data collection and PROFIT[19] and SHELX[20,21] for data reduction, Gaussian absorption correction, and initial structure refinement. X-ray refinements used the locally developed program ASRED,[22] and Fourier maps and geometries were obtained using XTAL.[23] All refinements included corrections for multiple scattering, type II extinction, anomalous dispersion, and harmonic displacement parameters. The refinement proceeded on the basis of the electron density model outlined below. The quantity $\sum\{\sigma(I)^{-2}(I_{obs} - I_{calc})^2\}$ was minimized until the maximum shift/esd ratio was 0.01.

Electron Density Modeling. Refinement of the X-ray data with the conventional multipole or valence model of the electron density and the usual radial parameters consistently showed unsatisfactory features, just as in the CuTS case.[4] High- and low-angle refinements gave differing thermal parameters, and the total electron count was too high. As with CuTS, we adopted an augmented hybrid of a valence and multipole electron models to correct these features. The augmented model used here was identical to that used for CuTS,[4] itself a simple augmentation of a valence model described by Figgis et *al.*[24] This model attempts by the use of chemical constraints to minimize the number of refineable parameters. This reduces the refined number of parameters, for the given level of multipoles, from 495 to 274, and is decribed in more detail in ref 4. Here we summarize the main features of the model.

The difference between a valence model and the corresponding multipole model is in the different treatment of the spherical harmonic components of the atom-centered form factors, but the atom centered form factors are summed in the same way in both to provide calculated reflection intensities.

For a multipole model the atomic fragment form factor, $f(\kappa)$, is defined as

$$f(\kappa) = f_{core}(|\kappa|) + \sum_{nln'l'} \sum_{l''m''} c^{nln'l'}{}_{l'm''} Y^{l''}{}_{m''}(\theta,\phi) \langle j^{nln'l'}{}_{m''}(|\kappa|)\rangle$$

where $f_{core}(|\kappa|)$ is the core form factor, nl and $n'l'$ are two sets of atomic quantum numbers, and there are sets of multipoles specified by l'' up to order m''. The $c^{nln'l'}{}_{l''m''}$ are refinable coefficients, and the $Y^{l''}{}_{m''}(\theta,\phi)$ are spherical harmonics defined with the phase convention of Condon and Shortley.[25] In this case we choose a definition of the shell form factors, $\langle j^{nln'l'}{}_{m''}(|\kappa|)\rangle$, in terms of the overlap of the radial parts of two atomic orbitals $R_{nl}(r)$ of quantum numbers nlm'' and $n'l'm''$ and the spherical Bessel function $J_{m''}(|\kappa|r)$ of order m''.

$$\langle j^{nln'l'}{}_{m''}(|\kappa|)\rangle = \int r^2 R_{nl}(r) R_{n'l'}(r) J_{m''}(|\kappa|r)\, dr$$

The functions $R_{nl}(r)$ are obtained from ref 26, and the shell and core form factors calculated from these using the program JCALC.[27] The shell radial functions used are 3d and 4p on Fe, 2p on N and O, and 3p on S.

For all the atom centers except iron we have used a multipole formulation to order 4 on S, N, and O and 2 on D. Imposition of local symmetry is then simple. We have imposed $\bar{4}3$ local symmetry on N and S, mirror symmetry on O(7)−O(9)− with the mirror plane defined as the D_2O plane, cylindrical symmetry about the bond on O(3) to O(6) and the deuteriums, and no constraint on the Fe site.

The disadvantage of a multipole model formulated in this way is that it is an expansion in reciprocal space. But quantum chemistry conventionally expresses wave functions in terms of valence bases in real space. Thus it is difficult to build into the multipole expansion all the insights gained by theoretical chemistry, since the Fourier transform of the valence in real space is in reciprocal space a linear combination of multipoles, and vice versa. In particular, on the iron site, there are mixing constraints, and we make comparison with the results of ligand-field theory. This is conveniently accomplished by use of a valence model.

In the valence model we refine coefficients of *multipolar electron distributions in real space* and their products. Using the standard three-j symbols $C^{l''m''}(lm,l'm')$[25,28] we can rewrite $f(\kappa)$ as

$$f(\kappa) = f_{core}(|\kappa|) + \sum_{nlmn'l'm'} \sum_{l''m''} c^{nlmn'l'm'} [8m'' + 4]\pi i^{m''} C^{l''m''}(lm,l'm') \times Y^{l''}{}_{m''}(\theta,\phi) \langle j^{nln'l'}{}_{m''}(|\kappa|)\rangle$$

where $c^{nlmn'l'm'}$ are refinable coefficients.

Thus in the valence model on the iron site we can refine terms such as the amount of overlap in real space of a $3d_{xy}$ and a $3d_{z^2}$ orbital—which we will write in this paper as $\langle xy|z^2\rangle$. In that case for example the scattering function $f(\kappa)$ contains j_0, j_2, and j_4 terms in a fixed ratio. In the limit when we consider *all* valence overlap terms or *all* multipoles arising from those valence terms the two methods of refinement are

(18) Henriksen, K.; Larsen, F. K.; Rasmussen, S. E. *J. Appl. Crystallogr.* **1986**, *19*, 390−394.
(19) Streltsov, V. A.; Zavodnik, V. E. *Sov. Phys. Crystallogr.* **1989**, *34*, 824−828.
(20) Sheldrick, G. M. *Acta Crystallogr., Sect. A* **1990**, *46*, 467−473.
(21) Sheldrick, G. M. *SHELXL97. Program for the Refinement of Crystal Structures.*; University of Göttingen: Germany, 1997.
(22) Figgis, B. N.; Williams, G. A.; Reynolds, P. A. *J. Chem. Soc., Dalton Trans.* **1980**, 2339−2347.
(23) Hall, S. R., King, G. S. D., Stewart, J. M., Eds. *XTAL3.4 Users Manual*; University of Western Australia, 1996.
(24) Figgis, B. N.; Reynolds, P. A.; Wright, S. *J. Am. Chem. Soc.* **1983**, *105*, 434−440.
(25) Condon, E. V.; Shortley, G. H. *The Theory of Atomic Spectra*; Cambridge University Press: Cambridge, U.K., 1957.
(26) Clementi, E.; Roetti, C. *At. Data Nucl. Data Tables* **1974**, *14*, 177−478.
(27) Figgis, B. N.; Reynolds, P. A.; White, A. H. *J. Chem. Soc., Dalton Trans.* **1987**, 1737−1745.
(28) Weiss, R. J.; Freeman, R. J. *J. Phys. Chem. Solids* **1959**, *10*, 147−161.

identical. Thus there are 15 overlap terms between the five d orbitals and a total of 15 multipoles of orders 0, 2, and 4. However, a chemical consideration is that the two e_g orbitals are expected to be energetically well separated from the three t_{2g} orbitals. Thus the six terms, such as $\langle d_{xy}|d_{z^2}\rangle$, involving t_{2g} overlap with e_g are expected to be small. These six terms involve all the zero-order, second-order, and fourth-order multipoles and are thus very difficult to neglect in a traditional multipole refinement, but this process is simple in a valence refinement. In this case the only functions with a 3d radial dependence that we have refined on the Fe site are the nine 3d overlap densities to allow for full reorientation of the t_{2g} electron density, *viz*. $\langle xy|xy\rangle$, $\langle xz|xz\rangle$, $\langle yz|yz\rangle$, $\langle xy|xz\rangle$, $\langle xy|yz\rangle$, $\langle xz|yz\rangle$, $\langle x^2-y^2|x^2-y^2\rangle$, $\langle z^2|z^2\rangle$, and $\langle x^2-y^2|z^2\rangle$. We have replaced all the multipole terms on the iron site with valence terms. We define the *z* axis as the Fe−O(7) direction, and the *xz* plane as the Fe−O(7)−O(8) plane, and so *x* is almost along Fe−O(8) and *y* almost along Fe−O(9).

While such a refinement is adequate for the non-hydrogen atoms, the lack of core electron density for hydrogen significantly biases the estimates of deformation densities and derived quantities. Accordingly we used deuterium positions and displacement parameters from the neutron diffraction data in the refinement. Thus we have adopted a partial X-ray−neutron (X−N) refinement. We added two Slater-type orbital radial distributions on each deuterium site (1s $\zeta = 1.0$ and 0.5). We used three cylindrical multipoles to describe the angular behavior of $\zeta = 1.0$ (00, 10, 20) and a spherical function only for $\zeta = 0.5$.

Lastly we have allowed radial changes in the multipole functions and Fe(3d) by use of κ refinement[29] and added a spherical Gaussian electron density of width 0.16 Å^2 at the midpoint of all seven chemical bonds involving oxygen.

This model, essentially a usual multipole model, is still not adequate to fit these data. Just as with CuTS,[4] high- and low-angle refinements give different scales and thermal parameters. The model strongly prefers an incorrect number of electrons in the cell, and residual maps show definite features. Suggested by the latter, we augmented the model by additional spherical functions. On each O and N site we added two functions transferring density from diffuse to less diffuse regions of the atom, but only a single extra such function on the S sites. These functions provide a means of changing the diffuse radial dependence independently of κ, and differently from it. The Fe valence distribution did not need modifying in this way, since the diffuse 4p function was already present.

The augmenting functions' radial dependences are defined in terms of Slater orbitals with exponents given by the two most diffuse bases in the atomic calculations,[26] which we call $|S1\rangle$ and $|S2\rangle$, where $|S1\rangle$ is the most diffuse. On all N, O, and S we refine coefficients of a density $[\langle S1|S1\rangle - \langle S1|S2\rangle]$, while on O and N we also refine the coefficient of $[\langle S1|S2\rangle - \langle S2|S2\rangle]$.

This model is now satisfactory. High- and low-angle refinements give similar thermal parameters and scales, use of the correct cell electron count does not degrade the fit, the agreement factor improves somewhat, and residual density maps are almost featureless. Surprisingly the net effect on the deformation maps of these extra diffuse functions is to allow the other functions to produce contracted minima near the nuclei.

This model gives agreement factors χ^2 1.14 and $R(F)$ 0.0094 (Table 1). Table 2 shows positional and displacement parameters for the non-hydrogen atoms, while Table 3 shows some significant bond lengths and angles using this combination of X-ray-derived heavy-atom coordinates and neutron deuterium coordinates, which form the most reliable and accurate set. Table 4 shows all the electronic parameters associated with the Fe site; the rest are given in the Supporting Information.

Addition of fourth- and third-order Gram−Charlier anharmonic displacement parameters to the Fe and S sites, respectively, does not improve the fit significantly, and none of the parameters refine to significant values. We expect this from the neutron result and also since at these low temperatures we expect only very small anharmonicity. The correlation of the anharmonic parameters with the most contracted electron modeling functions was small.

(29) Coppens, P.; Guru-Row, T. N.; Leung, P.; Stevens, E. D.; Becker, P.; Yang, Y. W. *Acta Crystallogr. Sect. A* **1979**, *35*, 63−72.

Table 2. X-ray and Neutron Positional Parameters ($\times 10^5$) and Displacement Parameters (Å$^2 \times 10^4$)[a]

atom	*x*	*y*	*z*
Fe	0	0	0
	0	0	0
S(2)	41270(10)	13005(8)	73500(20)
	41258(1)	13008(1)	73494(1)
O(3)	42077(6)	22191(4)	58673(9)
	42059(1)	22190(1)	58660(2)
O(4)	55248(6)	06593(5)	78070(10)
	55240(2)	06614(1)	78073(2)
O(5)	28043(6)	06193(5)	61899(9)
	28035(2)	06195(1)	61893(2)
O(6)	38997(6)	17261(5)	94293(9)
	38991(1)	17268(1)	94305(3)
O(7)	17987(6)	10740(5)	17014(9)
	17965(3)	10748(2)	17007(2)
O(8)	−16430(6)	11720(5)	02990(10)
	−16424(2)	11711(2)	02979(4)
O(9)	−00097(6)	−07099(5)	30234(9)
	−00095(2)	−07090(1)	30217(3)
N(10)	13614(4)	34040(3)	35194(6)
	13618(2)	34044(1)	35193(2)
D(11)	07000(10)	33006(9)	19130(10)
D(12)	22970(10)	29112(8)	38830(20)
D(13)	06980(10)	32147(8)	45330(20)
D(14)	16990(10)	42015(7)	37310(20)
D(15)	22690(10)	08765(8)	32480(20)
D(16)	26030(10)	11789(8)	10000(20)
D(17)	−26865(10)	10038(7)	−05940(20)
D(18)	−14880(10)	19151 (7)	−00660(20)
D(19)	−09590(10)	−06119(8)	34120(20)
D(20)	02560(10)	−14727(7)	32850(20)

	U_{11}	U_{22}	U_{33}	U_{12}	U_{13}	U_{23}
Fe(l)	38(1)	38(1)	35(1)	−1(1)	11(1)	4(1)
	37(1)	38(1)	46(1)	−1(1)	12(1)	1(1)
S(2)	35(3	36(3)	35(3)	−1(2)	12(2)	−3(2)
	38(1)	39(1)	44(1)	−1(1)	12(1)	−1(1)
O(3)	81(2)	46(2)	61(2)	−1(1)	28(1)	9(1)
	81(1)	56(1)	69(1)	−6(1)	28(1)	9(1)
O(4)	52(2)	67(2)	85(2)	14(1)	11(1)	0(1)
	52(1)	76(1)	100(1)	16(1)	14(1)	−1(1)
O(5)	53(2)	57(2)	64(2)	−12(1)	14(1)	−6(1)
	54(1)	64(1)	72(1)	−14(1)	14(1)	−9(1)
O(6)	83(2)	65(2)	51(2)	−1(1)	27(1)	−9(1)
	87(1)	67(1)	58(1)	−1(1)	28(1)	−8(1)
O(7)	67(2)	73(2)	63(2)	−12(1)	16(1)	−2(1)
	66(1)	82(1)	70(1)	−12(1)	15(1)	−2(1)
O(8)	62(2)	58(2)	87(2)	4(1)	23(1)	0(1)
	63(1)	63(1)	94(1)	5(1)	22(1)	2(1)
O(9)	80(2)	59(2)	65(2)	6(1)	32(1)	10(1)
	78(1)	66(1)	75(1)	6(1)	35(1)	11(1)
N(10)	78(1)	68(1)	74(1)	1(1)	27(1)	0(1)
	76(1)	72(1)	79(1)	0(1)	27(1)	0(1)
D(11)	228(4)	245(4)	112(3)	−54(3)	20(2)	−18(2)
D(12)	149(3)	168(3)	281(4)	60(3)	76(3)	20(3)
D(13)	188(3)	215(3)	168(3)	0(3)	107(3)	20(3)
D(14)	214(3)	108(3)	213(4)	−27(2)	54(3)	−9(2)
D(15)	169(3)	187(3)	106(3)	−11(2)	12(2)	19(2)
D(16)	147(3)	212(3)	165(3)	−35(2)	81(2)	−12(2)
D(17)	101(2)	155(3)	181(3)	−6(2)	16(2)	−12(2)
D(18)	170(3)	96(2)	200(3)	−17(2)	62(2)	10(2)
D(19)	157(3)	184(3)	193(3)	35(2)	102(2)	24(2)
D(20)	184(3)	102(2)	177(3)	28(2)	66(2)	21(2)

[a] Neutron first entry, X-ray second, except only neutron data for D sites.

Results

Nuclear Structure. The hydrogen bonding and ionic structures in the Tutton salts have been discussed many times,

Table 3. Bond Lengths (Å) and angles (deg) from a Combined X−N Coordinate Set

	Bond Lengths		
Fe−O(7)	2.1502(3)	S−O(3)	1.4901(2)
Fe−O(8)	2.1385(3)	S−O(4)	1.4622(3)
Fe−O(9)	2.1009(3)	S−O(5)	1.4857(3)
O(7)−D(15)	0.9784(6)	S−O(6)	1.4843(3)
O(7)−D(16)	0.9722(10)	N−D(11)	1.0282(6)
O(8)−D(17)	0.9825(7)	N−D(12)	1.0238(10)
O(8)−D(18)	0.9799(9)	N−D(13)	1.0282(13)
O(9)−D(19)	0.9770(11)	N−D(14)	1.0333(9)
O(9)−D(20)	0.9806(9)		
	Bond Angles		
O(7)−Fe−O(8)	89.53(2)	O(3)−S−O(4)	109.93(1)
O(7)−Fe−O(9)	90.54(1)	O(3)−S−O(5)	107.81(1)
O(8)−Fe−O(9)	89.46(1)	O(3)−S−O(6)	109.03(1)
Fe−O(7)−D(15)	113.41(6)	O(4)−S−O(5)	109.50(2)
Fe−O(7)−D(16)	115.37(5)	O(4)−S−O(6)	110.87(1)
Fe−O(8)−D(17)	113.58(5)	O(5)−S−O(6)	109.65(1)
Fe−O(8)−D(18)	116.10(7)	D(11)−N−D(12)	111.38(9)
Fe−O(9)−D(19)	114.37(7)	D(11)−N−D(13)	107.26(8)
Fe−O(9)−D(20)	119.52(5)	D(11)−N−D(14)	108.48(9)
D(15)−O(7)−D(16)	108.07(7)	D(12)−N−D(13)	109.28(9)
D(17)−O(8)−D(18)	106.12(7)	D(12)−N−D(14)	110.09(7)
D(19)−O(9)−D(20)	105.79(8)	D(13)−N−D(14)	110.31(9)

Table 4. Decomposition of the Experimental Electron Density around the Iron Site into Valence Populations (e)

	population	
valence function	expt	ligand-field theory
3d		
$\langle xy\|xy\rangle$	1.06(2)	1.24
$\langle yz\|yz\rangle$	1.06(2)	1.19
$\langle xz\|xz\rangle$	1.46(2)	1.57
$\langle xy\|yz\rangle$	−0.19(2)	−0.42
$\langle xy\|xz\rangle$	−0.46(2)	−0.74
$\langle xz\|yz\rangle$	0.38(2)	0.66
$\langle x^2-y^2\|x^2-y^2\rangle$	0.93(2)	
$\langle z^2\|z^2\rangle$	0.95(2)	
$\langle x^2-y^2\|z^2\rangle$	−0.11(2)	
3d radius	0.944(4)	
4p		
$\langle x\|x\rangle$	1.33(17)	
$\langle y\|y\rangle$	0.64(17)	
$\langle z\|z\rangle$	1.53(17)	

so here we note only the improved accuracy of our bond lengths and angles compared to the results of refs 11 and 12, which *inter alia* further confirms the small but significant deviation from tetrahedral stereochemistry for the sulfate and ammonium ions, apparently resulting from hydrogen bonding within the crystal.

However, if we turn to the displacement parameters, we see no such evidence of intermolecular effects. In Figure 1 we have plotted three hydrogen-bond-connected hexaaquairon(II), ammonium, and sulfate fragments from the unit cell in the *bc* projection. To render the small displacements easily visible we have plotted 90% rather than the usual much smaller 50% surfaces. It is well-known that zero-point motion, such as we are seeing here, is dominated by intramolecular vibrational modes,[30] unlike high-temperature thermal motion where intermolecular motion predominates. Thus, we can make the predictions which follow: (1) For Fe, S(2), and N(10) we should see relatively small and isotropic thermal ellipsoids. (2) All the O and H principal axes should be aligned with local bonding symmetry. (3) Terminal atoms (O(3)−O(6) and all D) should

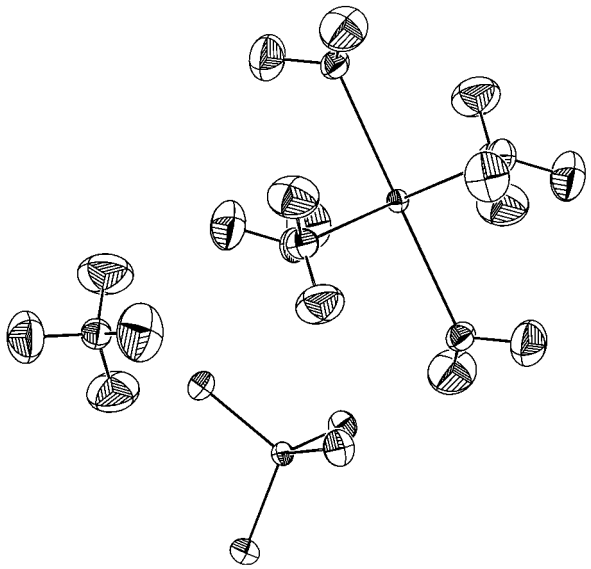

Figure 1. Displacements in molecular fragments, ORTEP *bc* projection, 90% ellipsoids of three hydrogen-bonded hexaaquairon(II), ammonium, and sulfate ions. The sulfate is at the bottom.

be relatively isotropic perpendicular to the bond, and due to the relative frequencies of bond stretching and bending, motion perpendicular to the bond should exceed that parallel to it. (4) Due to its low mass the deuterium motion should greatly exceed that for the heavy atoms. All of these predictions are borne out by experiment. Since these motions are so small, this is an excellent internal test of the reliability of the data and its interpretation. We note that these requirements are MORE stringent than the bond rigidity tests that are commonly used at higher temperatures. A further point to note is that the use of deuterated materials, besides providing the advantage of reducing incoherent scattering background in the neutron diffraction experiment, reduces the zero-point motion at the hydrogen sites by a factor of about $\sqrt{2}$. This allows better definition of the charge flows around these sites. The only cost in this case was simple final recrystallizations from D_2O.

A further internal test of the data is to compare the X-ray and neutron positional and displacement parameters for the non-H atoms. Since these are independently derived their agreement, or otherwise, provides a demanding check on data quality and processing methodology. The agreement between neutron and X-ray positional parameters is excellent (Table 2, top). The agreement in displacement parameters is also good (Table 2, bottom)—the mean absolute difference between X-ray and neutron diagonal thermal elements is 0.0005 Å^2, a 9% percentage error in an already small number. This agreement, while marginally worse than for CuTS, is acceptable and significantly better than many other accurate X−N studies.[31] However these X−N differences ARE significant. While U_{11} and the off-diagonal elements agree well, both U_{22} and U_{33} are consistently larger for the X-ray experiment. The worst agreement is for U_{33} on Fe, where $[U_{33}(\mathrm{N}) - U_{33}(\mathrm{X})]/[\sigma^2(U_{33}(\mathrm{N}) + \sigma^2(U_{33}(\mathrm{X})]^{1/2}$, the significance of the difference, is 8. Even at 10 K there remain uncorrected systematic errors. While thermal diffuse scattering and anharmonicity may be essentially removed, we still have, for example, scan truncation and multiple scattering errors as a possibility. This is the reason that for electron density calculations we use the displacement parameters derived from the X-ray results.

(30) Willis, B. T. M.; Pryor, A. W. *Thermal vibrations in crystallography*; Cambridge University Press: Cambridge, U.K., 1975.

(31) Iversen, B. B.; Larsen, F. K.; Figgis, B. N.; Reynolds, P. A.; Schultz, A. J. *Acta Crystallogr., Sect. B* **1996**, *52*, 923−931.

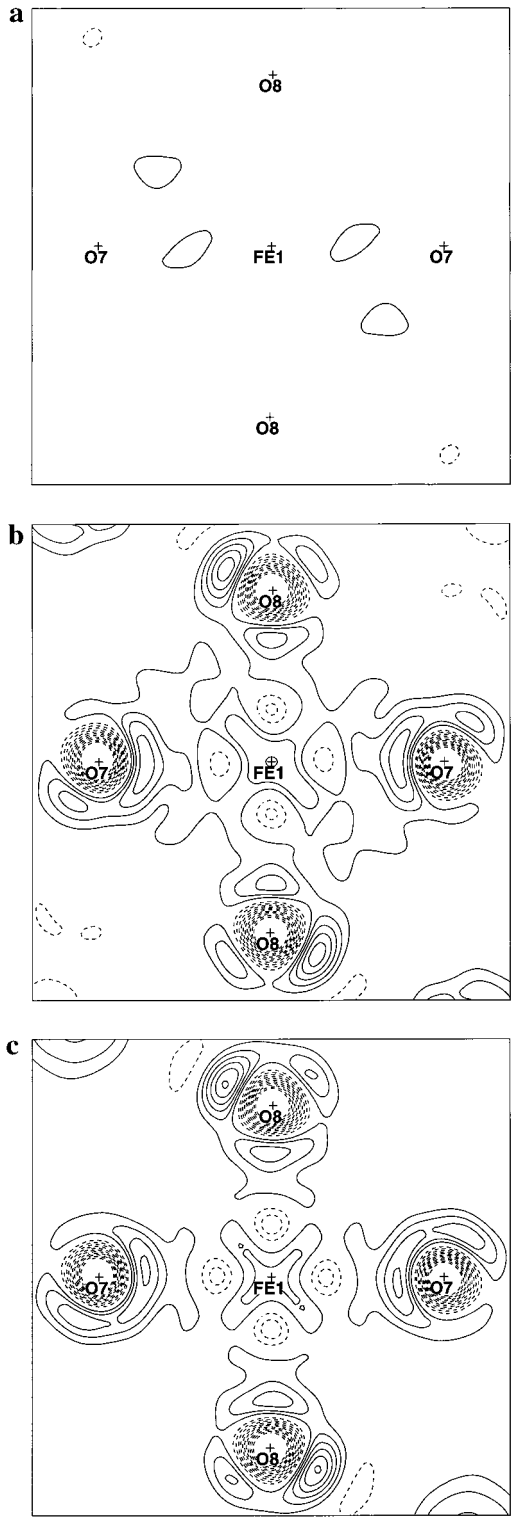

Figure 2. (a) Residual density in the Fe−O(7)−O(8) plane. (b) Deformation density in the Fe−O(7)−O(8) plane. (c) Model density in the Fe−O(7)−O(8) plane. The contour interval is 0.1 e Å^{-3}, zero suppressed, solid positive, dashed negative; the same in all subsequent contour plots. Box size is 5.98 Å, and resolution is to 0.7 Å^{-1}.

Electron Density Maps. Figure 2a shows the residual density in the hexaaquairon(II) ion in the Fe−O(7)−O(8) plane after fitting our best model to the data, as calculated to a resolution of 0.7 Å^{-1}. Figure 2b shows the deformation density, defined as the difference between the observed density and that of a superposition of free atoms, and thus showing electron density changes consequent on bonding. Figure 2c shows the model difference density, the difference of our fitted model density, and a superposition of free atoms for this same plane. As with the CuTS case, these maps show the features, which hold for all planes in the crystal, that the residual density is very small and that the deformation and model difference densities are almost the same. This means that our multipole model is, to within our experimental accuracy, complete. Thus we shall subsequently only discuss the deformation maps. Static model maps are sometimes used to display electron density experimental results. In these the modeled electron density is used while the nuclear displacement parameters are set to zero. This can be misleading since it can display density features assumed in the model which are removed by thermal motion and thus not tested against the data. We prefer the deformation density, since although it contains both experimental noise and zero-point thermal motion, it does not perform a possibly unsound deconvolution.

When we compare the deformation maps in the sulfate, ammonium, and water fragments with the corresponding published CuTS maps[4] we notice that they are extremely similar, so similar that we reproduce them in this case only in the Supporting Information. This reproducibility both across chemically different crystals and across different X-ray and neutron diffractometers, together with the theoretical agreement shown in ref 6, provides further strong evidence for the reality of deformation features observed around the iron atom site in this study.

All of the deformation maps, due to limitations of the contouring routine used, are truncated at a lower value of −1.1 e Å^{-3}, so as not to limit the positive contouring. As with the CuTS data this truncates low values of the deformation density at the non-metal nuclei. These values for the deformation density reach −1.6(2) to −1.7(2) for O(3) to O(6) [−2.3(2) to −2.3(2)], −1.7(2) to −1.8(2) for O(7) to O(9) [−2.2(2) to −2.5-(2)], −1.2(2) for N(10) [−1.4(2)], and 0.0(4) e Å^{-3} for S(2)[−1.4(4)]. Corresponding values for CuTS[4] are given in square brackets. Such values of electron depletion near the nucleus caused by bonding are reproduced by theoretical calculations[4,6] and are revealed in these data because of the low thermal motion and more reliable estimates of the overall scale factor.[4]

Figure 3a−d shows further deformation densities in four planes through the iron site. The major feature is an electron deficit, relative to a spherical $3d^6 4s^2$ neutral iron atom reaching −0.72 e Å^{-3} at a distance of 0.48 Å along the Fe−O(9) bond from Fe. This is shown in Figure 3a,b. Figure 2b shows only slight changes in the Fe−O(7)−O(8) plane, indicating an almost uniaxial deformation. These three planes do not intersect any formally 3d t_{2g} symmetry density. Five of the six such planes show no features; an example is Figure 3d. However, one plane containing Fe, O(7), and the mean coordinate of O(8) and O(9) does show a maximum in the deformation density almost along the direction [−O(7) + O(8) + O(9)] of +0.32 e Å^3 at 0.73 Å from the iron site. This is shown in Figure 3c. The amount of positive charge contained in this deformation peak is smaller than the deficit in the hole along Fe−O(9). Thus, to a good approximation, the deformation density around the Fe site follows the local oxygen environment in symmetry, where Fe−O(9) at 2.1009(3) Å is distinctly shorter than the more equal Fe−O(7) (2.1502(3)) and Fe−O(8) (2.1385(3)). This depletion of density at a shorter bond is just as we might expect.

There is a slight, but significant, deviation of the deformation density on the iron atom from local symmetry. The direction of this, [−O(7) + O(8) + O(9)], does not correspond to the rough S_6 axis ([O(7) + O(8) + O(9)]) produced by putting all

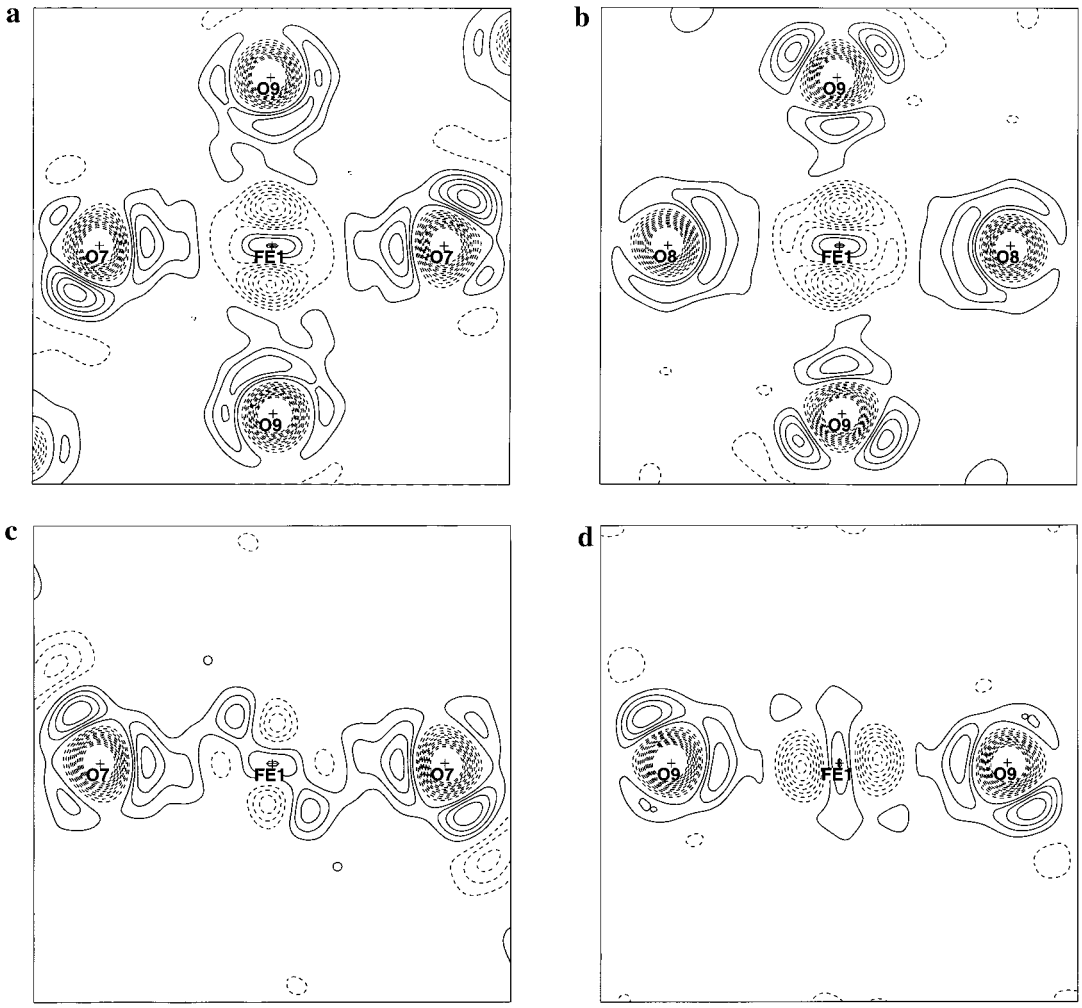

Figure 3. Deformation density maps: (a) Fe−O(7)−O(9); (b) Fe−O(8)−O(9); (c) Fe−O(7)−mean of O(8) and O(9); (d) Fe−O(9)−mean of O(7) and O(8).

the water molecules twists, tilts, and yaws to zero.[4] Nor does it correspond to nearest-neighbor Fe···Fe directions ([001] and [$^1/_2$,$^1/_2$,0]. It does however correspond approximately to the direction of the nearest sulfate ion, whose sulfur coordinate, 0.41, 0.13, −0.27, corresponds in direction with [O(7)−O(8)−O(9) (at 0.35, 0.06, −0.16). It is likely that this is an indirect effect, since the sulfate group produces an orienting of the water molecules by hydrogen bonding, which in turn will change the local π bonding regime from water onto the iron site. But it does seem to be an effect reflecting the crystal geometry. However the exact mechanism might only be clarified by theoretical calculations.

Discussion

Electron Density at the Iron Site and Local Nuclear Symmetry. The good agreement of the CuTS data with the *ab initio* calculations of the electron density around water, sulfate, and ammonium suggests that, although there may be some interesting bonding effects in these areas, the major feature in this present study to discuss is the density around the iron site. The model electron density parameters which reduce the modulus of the residual density around the iron site to less than 0.15 e Å^{-3} are listed in Table 4. This density is significantly different from octahedral symmetry. The 3d $\langle xz|xz\rangle$ component is larger than either $\langle xy|xy\rangle$ or $\langle yz|yz\rangle$. As already noted this reflects the polarizing effect of the Fe−O(9) bond, which is significantly shorter than Fe−O(8) or Fe−O(7). The diffuse density is also polarized in the same way by the ligating waters such that the smallest 4p population, $\langle y|y\rangle$, is that directed along the Fe−O(9) bond. This polarization and the shortness of the Fe−O(9) bond are correlated, just as in other Jahn−Teller systems. It is just as valid to say that the polarization reduces the electronic repulsion between water and iron, thus allowing the Fe−O(9) bond to shorten with respect to the other two independent Fe−O bonds. However, given the substantial polarization, shortness of the Fe−O(9) bond should NOT be taken to imply increased covalence over Fe−O(8) and Fe−O(7)—indeed the PND experiment[10] indicates a quite ionic Fe−O bonding. However in addition to this 3d polarization the off-diagonal terms ($\langle xy|yz\rangle$, $\langle xy|xz\rangle$, and $\langle xz|yz\rangle$) are also significant, meaning that there is electronic distortion to a symmetry lower than *mmm*.

Other workers have also reported deviations in the deformation density from local nuclear symmetry on the basis of data obtained at higher temperatures, but in many cases, we should be cautious about the interpretation. Where the thermal motion is high, errors in it, and neglect of the highly temperature dependent anharmonic contributions, will be compensated to some extent in the deformation density. Since the thermal motion at high temperatures strongly reflects intermolecular or crystal forces, then small errors in displacement parameters, already discussed as being likely at higher temperatures, may force an unreal nonlocal symmetry on the central metal

deformation density. References 32−34 may fall in this category. However, other work of the Uppsala group[35−37] does not do so, being at very low temperature. There deviation from local symmetry for the orbitally nondegenerate hexaaquanickel(II) ion is small but seemingly reliable and is even larger for the orbitally degenerate, and thus more polarizable, hexaaquacobalt(II) ion.

Ab Initio Calculations and Experimental Total 3d and 4s/p Populations. *Ab initio* calculations[8,13−15] vary somewhat in their predictions of the effect of bonding on the iron configuration.

The calculation of Chandler *et al.*[8] is a local density functional calculation in the unrestricted Hartree−Fock approximation with numerical basis functions fixed at atomic values; Mandix and Johansen[14] report *ab initio* Hartree−Fock multiconfigurational calculations in contracted configuration interaction approximation with about a double ζ level basis; Akesson *et al.*[13,15] used a multireference configuration interaction approximation (CASSCF) with similar level bases.

Chandler *et al.*[8] and Akesson *et al.*[13,15] predict that bonding significantly increases the metal-centered 4s plus 4p populations, to 0.72 and 0.37 e, respectively, while the 4s and 4p population of Mandix and Johansen[14] is smaller at 0.10 e. Akesson *et al.* predict a small decrease in 3d electron populations to 5.91 e due to hybridization with the 4s density, while both Chandler and Mandix calculate a small 3d population increase to 6.16 and 6.05 e, respectively.

We actually observe a significant decrease in 3d population to 5.46(5) e and a very large diffuse 4s/p population of 3.50(25) e. It would thus appear that the *ab initio* theories agree with experiment in placing density gained from the water ligand by bonding predominantly in the diffuse 4s and 4p region. In particular the e_g population of 1.88(4) e is decreased from the crystal field ionic value of 2.00 e, presumably because, in spite of donation of electrons from the oxygen into these σ-bonding orbitals, increased 4s participation more than compensates for this. The reduction in 3d radial extent of 5.6(4)% is consistent with decreased mutual shielding of remaining 3d electrons. Insofar as we can compare least-squares orbital populations with the Mulliken populations of theoretical chemistry, theory underestimates both the 4s/p populations and the 3d/4sp hybridization dramatically. The 4s and p density is sufficiently diffuse, and the oxygen-based functions sufficiently contracted that a strict division into Fe- and O-based density is not valid. The 4s and p density could well include density arising from oxygen in a theoretical wave function. The experiment on CuTS produces a slightly different picture, with less diffuse density and a slight increase in 3d population above 9.00 e, whereas the theories do not change in their predictions much from Fe to Cu. Given the reproducibility of other features, such as sulfate density, we suspect that this difference in bonding is also real.

Ligand Field Theory and Anisotropy in the Experimental 3d Population. The *ab initio* calculations are all nonrelativistic, and the previous ligand-field model[9] indicates that spin−orbit coupling cannot be neglected in the consideration of the anisotropy of the 3d electronic distribution. Thus these *ab initio* calculations cannot be directly compared with our experimental *anisotropy* in the 3d distribution. The *ab initio* calculations produces three closely spaced 5-fold degenerate states of differing angular distribution of 3d electrons, which spin−orbit coupling will further mix to give a manifold of 15 states. To obtain a theoretical estimate of the anisotropy in this ground state we must resort to ligand-field theory to calculate these 15 states' energies and natures.

Providing the 3d configuration is relatively close to that of the free ion, ligand-field theory can be used. However, we must note that it provides no firm estimate of the total 3d population, since it accounts for their population changes indirectly, by adjustment of energy parameters. The experiment shows small changes in the t_{2g} and e_g 3d populations from those for an Fe(II) ion in an octahedral field. The e_g population changes from 2 to 1.88(4) and the t_{2g} from 4 to 3.58(4). These are acceptably close to free ion values so as to allow use of a ligand-field theory.

Doerfler's crystal-field model makes a prediction for the ground-state unpaired spin molecular orbital as

$$\Psi = -0.489|xy\rangle + 0.432|yz\rangle + 0.757|xz\rangle$$

This is produced by the energy of $|xy\rangle$ higher than $|xz\rangle$ by 490 cm^{-1} and $|yz\rangle$ by 220 cm^{-1}, together with the principal axis rotated about 41° away from Fe−O(9) bond axis in the Fe−[(O(8)−O(7))] direction. The spin−orbit coupling has been reduced to 88% of the free ion value. Other ligand-field models, referred to in ref 9, have roughly similar energy level ordering but lack the rotation.

Table 4 shows some agreement between the predictions of this ligand-field theory's ground state and the six observed t_{2g} populations. At 10 K the experiment is sampling 72% of the ground state and 28% of the first, 6.4 cm^{-1}, excited state. However the ligand-field theory also predicts almost identical t_{2g} populations for both these states, so a comparison of observed and calculated terms is still valid. The agreement is good—the ligand field predicts diagonal elements some 10% higher than observed. But, as we have already noted, the ligand-field population of 4 in the t_{2g} is an overestimate. The anisotropy is however well reproduced.

The three calculated off-diagonal elements have the same sign and ordering as is observed but are overestimated by the theory. Given the low symmetry of the site, the agreement in sign and order is impressive. We can explore this further by attempting to construct an experimental unpaired spin molecular orbital.

From the experimental off-diagonal overlap populations we can deduce an experimental unpaired spin molecular orbital

$$\Psi = -0.338|xy\rangle + 0.277|yz\rangle + 0.738|xz\rangle + ...$$

where the ... implies further, non-3d, contributions.

This predicts diagonal orbital spin populations of $\langle xy|xy\rangle = 0.08$, $\langle xz|xz\rangle = 0.54$, and $\langle yz|yz\rangle = 0.11$ e and a total 3d population participation in the orbital of 0.73 e. These numbers agree reasonably well with those observed, where we see $\langle xz|xz\rangle$ exceeding $\langle xy|xy\rangle$ by 0.40(3) e and with $\langle xy|xy\rangle$ equaling $\langle yz|yz\rangle$ in population. The total 3d population if carried across all four original t_{2g} ionic orbitals gives a molecular t_{2g} population of 2.94 e, rather less than the 3.58(4) observed experimentally.

Comparison of the experimental and theoretical orbitals shows similarity in the coefficients. However, ligand-field theory is essentially a theory about *angular* distributions. As we have noted covalence is dealt with in a distinctly *ad hoc* manner. A

(32) Maslen, E. N.; Ridout, S. C.; Watson, K. J. *Acta Crystallogr., Sect. B* **1988**, *44*, 96−101.
(33) Hester, J. R.; Maslen, E. N.; Glazer, A. M.; Stadnicka, K. *Acta Crystallogr., Sect. B* **1993**, *49*, 641−646.
(34) McIntyre, G. J.; Ptasiewicz-Bak, H.; Olovsson, I. *Acta Crystallogr., Sect. B* **1990**, *46*, 27−39.
(35) Ptasiewicz-Bak, H.; Olovsson, I.; Mcintyre, G. J. *Acta Crystallogr., Sect. B* **1997**, *53*, 325−336.
(36) Ptasiewicz-Bak, H.; Olovsson, I.; Mcintyre, G. J. *Acta Crystallogr., Sect. B* **1993**, *49*, 192−201.
(37) Kellersohn, T.; Delaplane, R. G.; Olovsson, I.; McIntyre, G. J. *Acta Crystallogr., Sect. B* **1993**, *49*, 179−192.

more stringent test of the theory is to examine the direction of the observed maximum in the electron densities in space. The observed maximum in the electron density maps is in the direction given by conventionally defined polar angles as $\theta = 37(2)°$ and $\vartheta = 135(5)°$. This compares well to the ligand-field-model values of 41(1)° and 139(2)° The experimentally derived unpaired spin molecular orbital implies polar angles of $\theta = 31(2)°$ and $\vartheta = 141(2)°$, close to both those predicted in the ligand-field model and those deduced from the raw deformation maps.

Thus the observed t_{2g} populations confirm the main features of the complete ligand-field model, particularly the angular consequences, and subject to the proviso that there are substantial radial changes in electron distribution associated with bonding.

At 85 K the first five states all are appreciably populated while the next 10 are not, and given the higher thermal motion, a static model is not so appropriate. The first five states are calculated by Doerfler's ligand-field theory to occupy a range of 99 cm^{-1}. Thus at 85 K the highest level has 56% of the occupation of the ground state. If all five lowest states were equally populated this model would predict that the three off-diagonal overlaps would be almost zero while we would obtain $\langle xz|xz\rangle = 1.8$ and $\langle xy|xy\rangle = \langle yz|yz\rangle = 1.1$. At 85 K the experiment does indeed show *mmm* symmetry in the deformation density around the Fe site[11] but has an excess of density along the *y* axis (Fe−O(9)), in disagreement with both the ligand-field prediction and naive expectations. This may be a sign that even at 85 K systematic errors are significant—as discussed above in the context of nonlocal symmetries. It may also, however, be a result of the fact that the vibronic effects connected dynamic Jahn−Teller effect may be operating. In either case the 85 K results lead to a suspicion that even that temperature is too high for critical comparison with theory in this salt.

Conclusion

From this work we see that at very low temperatures corrections to the electron density distribution for harmonic and anharmonic thermal motion and thermal diffuse scattering become so small that quite fine details about the ground state of a transition metal atom in a complex can be established. In the case of FeTS the electron distribution around the iron atom is quite anisotropic because it then has contributions from only two closely similar states. The previous data at 85 K are shown to be more limited, in that the distribution does not agree with the predictions of the model and may contain unavoidable systematic errors due to the higher temperature.

At very low temperatures the shape of the 3d electron density around the iron atom agrees well with that predicted from a variety of spectroscopic-type physical measurements via a wave function derived with the use of ligand-field theory. Since this involves a density considerably twisted away from the local ligand axis directions it implies that such ligand-field modeling, if complete enough, expresses real information concerning the molecular wave function.

We do however also observe that there is donation from both e_g and t_{2g} 3d orbitals into more diffuse orbitals on bonding. These diffuse orbitals increase considerably in population due to a larger contribution arising from donation from the ligating waters.

The work also provides a further example of the fact that, with the above corrections minimized by the very low temperature, the X-ray and neutron diffraction experiments lead to very similar atomic displacement parameters. This greatly increases the physical significance which can be attached to those parameters and means that they can be used with confidence in other applications.

Acknowledgment. This work has benefited from the use of the Intense Pulsed Neutron Source, Argonne National Laboratory. This facility is funded by the U.S. Department of Energy, BES-Materials Science, under Contract W-31-109-Eng-38. We also acknowledge financial support from the Australian Research Council and the Department of Industry, Science and Tourism. We are grateful to the reviewers for comments leading to considerable clarification in the discussion.

Supporting Information Available: Maps of the deformation, residual, and model density for the S(2)−O(3)−O(4) plane and the deformation density of N(10)−D(11)−D(12) and 0(7)−D(15)−D(16), and list of the results of the least-squares electron modeling calculation (7 pages, print/PDF). See any current masthead page for ordering information and Web access instructions.

JA9739805